



## Quality assessment of terahertz time-domain spectroscopy transmission and reflection modes for graphene conductivity mapping

Mackenzie, David M.A.; Whelan, Patrick Rebsdorf; Bøggild, Peter; Jepsen, Peter Uhd; Redo-Sanchez, Albert; Etayo, David; Fabricius, Norbert; Petersen, Dirch Hjorth

*Published in:*  
Optics Express

*Link to article, DOI:*  
[10.1364/OE.26.009220](https://doi.org/10.1364/OE.26.009220)

*Publication date:*  
2018

*Document Version*  
Publisher's PDF, also known as Version of record

[Link back to DTU Orbit](#)

### *Citation (APA):*

Mackenzie, D. M. A., Whelan, P. R., Bøggild, P., Jepsen, P. U., Redo-Sanchez, A., Etayo, D., Fabricius, N., & Petersen, D. H. (2018). Quality assessment of terahertz time-domain spectroscopy transmission and reflection modes for graphene conductivity mapping. *Optics Express*, 26(7), 9220-9229. <https://doi.org/10.1364/OE.26.009220>

---

### General rights

Copyright and moral rights for the publications made accessible in the public portal are retained by the authors and/or other copyright owners and it is a condition of accessing publications that users recognise and abide by the legal requirements associated with these rights.

- Users may download and print one copy of any publication from the public portal for the purpose of private study or research.
- You may not further distribute the material or use it for any profit-making activity or commercial gain
- You may freely distribute the URL identifying the publication in the public portal

If you believe that this document breaches copyright please contact us providing details, and we will remove access to the work immediately and investigate your claim.



# Quality assessment of terahertz time-domain spectroscopy transmission and reflection modes for graphene conductivity mapping

DAVID M. A. MACKENZIE,<sup>1,\*</sup> PATRICK R. WHELAN,<sup>1</sup> PETER BØGGILD,<sup>1</sup>  
PETER UHD JEPSEN,<sup>2</sup> ALBERT REDO-SANCHEZ,<sup>3</sup> DAVID ETAYO,<sup>3</sup> NORBERT  
FABRICIUS,<sup>4</sup> AND DIRCH HJORTH PETERSEN<sup>1</sup>

<sup>1</sup>Center for Nanostructured Graphene (CNG), Department of Micro- and Nanotechnology, Technical University of Denmark, DK-2800 Kongens Lyngby, Denmark

<sup>2</sup>Center for Nanostructured Graphene (CNG), Department of Photonics Engineering, Technical University of Denmark, DK-2800 Kongens Lyngby, Denmark

<sup>3</sup>das-Nano, Poligono Industrial, Talluntxe II Calle M – 10. 31192, TAJONAR, Spain

<sup>4</sup>Germany Karlsruhe Institute of Technology, Hermann-von-Helmholtz-Platz 1, 76344 Eggenstein-Leopoldshafen, Germany

\*[dmac@nanotech.dtu.dk](mailto:dmac@nanotech.dtu.dk)

**Abstract:** We present a comparative study of electrical measurements of graphene using terahertz time-domain spectroscopy in transmission and reflection mode, and compare the measured sheet conductivity values to electrical van der Pauw measurements made independently in three different laboratories. Overall median conductivity variations of up to 15% were observed between laboratories, which are attributed mainly to the well-known temperature and humidity dependence of non-encapsulated graphene devices. We conclude that terahertz time-domain spectroscopy performed in either reflection mode or transmission modes are indeed very accurate methods for mapping electrical conductivity of graphene, and that both methods are interchangeable within measurement uncertainties. The conductivity obtained *via* terahertz time-domain spectroscopy were consistently in agreement with electrical van der Pauw measurements, while offering the additional advantages associated with contactless mapping, such as high throughput, no lithography requirement, and with the spatial mapping directly revealing the presence of any inhomogeneities or isolating defects. The confirmation of the accuracy of reflection-mode removes the requirement of a specialized THz-transparent substrate to accurately measure the conductivity.

© 2018 Optical Society of America under the terms of the [OSA Open Access Publishing Agreement](#)

**OCIS codes:** (120.4290) Nondestructive testing; (160.4236) Nanomaterials; (300.6250) Spectroscopy, condensed matter; (300.6495) Spectroscopy, terahertz; (310.3840) Materials and process characterization; (310.6870) Thin films, other properties.

## References and links

1. H. J. Yoon, D. H. Jun, J. H. Yang, Z. Zhou, S. S. Yang, and M. M. C. Cheng, "Carbon dioxide gas sensor using a graphene sheet," *Sens. Actuators B Chem.* **157**(1), 310–313 (2011).
2. F. Schedin, A. K. Geim, S. V. Morozov, E. W. Hill, P. Blake, M. I. Katsnelson, and K. S. Novoselov, "Detection of individual gas molecules adsorbed on graphene," *Nat. Mater.* **6**(9), 652–655 (2007).
3. A. Cagliani, D. M. A. Mackenzie, L. K. Tschammer, F. Pizzocchero, K. Almdal, and P. Bøggild, "Large-area nanopatterned graphene for ultrasensitive gas sensing," *Nano Res.* **7**(5), 743–754 (2014).
4. Y.-M. Lin, K. A. Jenkins, A. Valdes-Garcia, J. P. Small, D. B. Farmer, and P. Avouris, "Operation of graphene transistors at gigahertz frequencies," *Nano Lett.* **9**(1), 422–426 (2009).
5. D. M. A. Mackenzie, A. Cagliani, L. Gammelgaard, B. S. Jessen, D. H. Petersen, and P. Bøggild, "Graphene antidot lattice transport measurements," *Int. J. Nanotechnol.* **14**(1–6), 226 (2017).
6. F. Schwierz, "Graphene transistors," *Nat. Nanotechnol.* **5**(7), 487–496 (2010).
7. J. Wu, M. Agrawal, H. A. Beceril, Z. Bao, Z. Liu, Y. Chen, and P. Peumans, "Organic Light-Emitting Diodes on Solution-Processed Graphene Transparent Electrodes," *ACS Nano* **4**(1), 43–48 (2010).
8. T.-H. Han, Y. Lee, M.-R. Choi, S.-H. Woo, S.-H. Bae, B. H. Hong, J.-H. Ahn, and T.-W. Lee, "Extremely efficient flexible organic light-emitting diodes with modified graphene anode," *Nat. Photonics* **6**(2), 105–110 (2012).

9. T. Sun, Z. L. Wang, Z. J. Shi, G. Z. Ran, W. J. Xu, Z. Y. Wang, Y. Z. Li, L. Dai, and G. G. Qin, "Multilayered graphene used as anode of organic light emitting devices," *Appl. Phys. Lett.* **96**(13), 133301 (2010).
10. M. Galbiati, A. C. Stoot, D. M. A. Mackenzie, P. Bøggild, and L. Camilli, "Real-time oxide evolution of copper protected by graphene and boron nitride barriers," *Sci. Rep.* **7**(2), 39770 (2017).
11. N. T. Kirkland, T. Schiller, N. Medhekar, and N. Birbilis, "Exploring graphene as a corrosion protection barrier," *Corros. Sci.* **56**, 1–4 (2012).
12. F. Yu, L. Camilli, T. Wang, D. M. A. Mackenzie, M. Curioni, R. Akid, and P. Bøggild, "Complete long-term corrosion protection with chemical vapor deposited graphene," *Carbon* **132**, 78–84 (2018).
13. F. H. L. Koppens, D. E. Chang, and F. J. García de Abajo, "Graphene plasmonics: A platform for strong light-matter interactions," *Nano Lett.* **11**(8), 3370–3377 (2011).
14. Q. Wang, C. Z. Li, S. Ge, J. G. Li, W. Lu, J. Lai, X. Liu, J. Ma, D. P. Yu, Z. M. Liao, and D. Sun, "Ultrafast Broadband Photodetectors Based on Three-Dimensional Dirac Semimetal Cd<sub>3</sub>As<sub>2</sub>," *Nano Lett.* **17**(2), 834–841 (2017).
15. X. Guo, W. Wang, H. Nan, Y. Yu, J. Jiang, W. Zhao, J. Li, Z. Zafar, N. Xiang, Z. Ni, W. Hu, Y. You, and Z. Ni, "High-performance graphene photodetector using interfacial gating," *Optica* **3**(10), 1066 (2016).
16. V. Miseikis, D. Convertino, N. Mishra, M. Gemmi, T. Mashoff, S. Heun, N. Haghighian, F. Bisio, M. Canepa, V. Piazza, and C. Coletti, "Rapid CVD growth of millimetre-sized single crystal graphene using a cold-wall reactor," *2D Mater.* **2**(1), 014006 (2015).
17. B. Luo, J. M. Caridad, P. R. Whelan, J. D. Thomsen, D. M. A. Mackenzie, A. Grubišić Čabo, S. K. Mahatha, M. Bianchi, P. Hofmann, P. U. Jepsen, P. Bøggild, and T. J. Booth, "Sputtering an exterior metal coating on copper enclosure for large-scale growth of single-crystalline graphene," *2D Mater.* **4**(4), 045017 (2017).
18. S. Dhingra, J. F. Hsu, I. Vlasiouk, and B. D'Urso, "Chemical vapor deposition of graphene on large-domain ultra-flat copper," *Carbon* **69**, 188–193 (2014).
19. M. Kim, A. Shah, C. Li, P. Mustonen, J. Susoma, F. Manoocheri, J. Riikonen, and H. Lipsanen, "Direct transfer of Wafer-scale graphene films," *2D Mater.* **4**(3), 035004 (2017).
20. P. R. Whelan, B. S. Jessen, R. Wang, B. Luo, A. C. Stoot, D. M. A. Mackenzie, P. Braeuninger-Weimer, A. Jouvray, L. Prager, L. Camilli, S. Hofmann, P. Bøggild, and T. J. Booth, "Raman spectral indicators of catalyst decoupling for transfer of CVD grown 2D materials," *Carbon* **117**, 75–81 (2017).
21. T. Yager, A. Lartsev, R. Yakimova, S. Lara-Avila, and S. Kubatkin, "Wafer-scale homogeneity of transport properties in epitaxial graphene on SiC," *Carbon* **87**(C), 409–414 (2015).
22. P. Bøggild, D. M. A. Mackenzie, P. R. Whelan, D. H. Petersen, J. D. Buron, A. Zurutuza, J. Gallop, L. Hao, and P. U. Jepsen, "Mapping the electrical properties of large-area graphene," *2D Mater.* **4**(4), 042003 (2017).
23. L. Gammelgaard, J. M. Caridad, A. Cagliani, D. M. A. MacKenzie, D. H. Petersen, T. J. Booth, and P. Bøggild, "Graphene transport properties upon exposure to PMMA processing and heat treatments," *2D Mater.* **1**(3), 1–6 (2014).
24. J. D. Buron, F. Pizzocchero, P. U. Jepsen, D. H. Petersen, J. M. Caridad, B. S. Jessen, T. J. Booth, and P. Bøggild, "Graphene mobility mapping," *Sci. Rep.* **5**(1), 12305 (2015).
25. J. D. Buron, D. M. A. Mackenzie, D. H. Petersen, A. Pesquera, A. Centeno, P. Bøggild, A. Zurutuza, and P. U. Jepsen, "Terahertz wafer-scale mobility mapping of graphene on insulating substrates without a gate," *Opt. Express* **23**(24), 30721–30729 (2015).
26. D. M. A. Mackenzie, J. D. Buron, P. R. Whelan, B. S. Jessen, A. Silajdžić, A. Pesquera, A. Centeno, A. Zurutuza, P. Bøggild, and D. H. Petersen, "Fabrication of CVD graphene-based devices via laser ablation for wafer-scale characterization," *2D Mater.* **2**(4), 045003 (2015).
27. J. D. Buron, D. H. Petersen, P. Bøggild, D. G. Cooke, M. Hilke, J. Sun, E. Whiteway, P. F. Nielsen, O. Hansen, A. Yurgens, and P. U. Jepsen, "Graphene conductance uniformity mapping," *Nano Lett.* **12**(10), 5074–5081 (2012).
28. P. R. Whelan, K. Iwaszczuk, R. Wang, S. Hofmann, P. Bøggild, and P. U. Jepsen, "Robust mapping of electrical properties of graphene from terahertz time-domain spectroscopy with timing jitter correction," *Opt. Express* **25**(3), 2725–2732 (2017).
29. R. E. Glover and M. Tinkham, "Conductivity of superconducting films for photon energies between 0.3 and 40kT<sub>c</sub>," *Phys. Rev.* **108**(2), 243–256 (1957).
30. D. M. A. Mackenzie, J. D. Buron, P. Boaggild, P. U. Jepsen, and D. H. Petersen, "Contactless graphene conductance measurements: the effect of device fabrication on terahertz time-domain spectroscopy," *Int. J. Nanotechnol.* **13**(8/9), 591 (2016).
31. D. M. A. Mackenzie, J. D. Buron, P. R. Whelan, J. M. Caridad, M. Bjergfelt, B. Luo, A. Shivayogimath, A. L. Smitshuysen, J. D. Thomsen, T. J. Booth, L. Gammelgaard, J. Zultak, B. S. Jessen, P. Bøggild, and D. H. Petersen, "Quality assessment of graphene: Continuity, uniformity, and accuracy of mobility measurements," *Nano Res.* **10**(10), 3596–3605 (2017).
32. L. J. van der Pauw, "A method of measuring the resistivity and Hall coefficient of lamellae of arbitrary shape," *Phillips Tech. Rev.* **20**(1), 220–224 (1958).
33. J. Náhlík, I. Kašpárková, and P. Fitl, "Study of quantitative influence of sample defects on measurements of resistivity of thin films using van der Pauw method," *Meas. J. Int. Meas. Confed.* **44**(10), 1968–1979 (2011).
34. J. Heo, H. J. Chung, S.-H. Lee, H. Yang, D. H. Seo, J. K. Shin, U.-I. Chung, S. Seo, E. H. Hwang, and S. Das Sarma, "Nonmonotonic temperature dependent transport in graphene grown by chemical vapor deposition," *Phys. Rev. B* **84**(3), 035421 (2011).

35. D. M. A. Mackenzie, K. Smistrup, P. R. Whelan, B. Luo, A. Shivayogimath, T. Nielsen, D. H. Petersen, S. A. Messina, and P. Bøggild, "Batch fabrication of nanopatterned graphene devices via nanoimprint lithography," *Appl. Phys. Lett.* **111**(19), 193103 (2017).
36. A. D. Smith, K. Elgammal, F. Niklaus, A. Delin, A. C. Fischer, S. Vaziri, F. Forsberg, M. Råsander, H. Hugosson, L. Bergqvist, S. Schröder, S. Kataria, M. Östling, and M. C. Lemme, "Resistive graphene humidity sensors with rapid and direct electrical readout," *Nanoscale* **7**(45), 19099–19109 (2015).
37. M. B. S. Larsen, D. M. A. Mackenzie, J. M. Caridad, P. Bøggild, and T. J. Booth, "Transfer induced compressive strain in graphene: Evidence from Raman spectroscopic mapping," *Microelectron. Eng.* **121**, 113–117 (2014).
38. A. C. Ferrari and D. M. Basko, "Raman spectroscopy as a versatile tool for studying the properties of graphene," *Nat. Nanotechnol.* **8**(4), 235–246 (2013).
39. W. Yuan and G. Shi, "Graphene-based gas sensors," *J. Mater. Chem. A Mater. Energy Sustain.* **1**(35), 10078 (2013).
40. I. Childres, L. A. Jauregui, J. Tian, and Y. P. Chen, "Effect of oxygen plasma etching on graphene studied using Raman spectroscopy and electronic transport measurements," *New J. Phys.* **13**(2), 025008 (2011).
41. D. W. Koon, F. Wang, D. H. Petersen, and O. Hansen, "Sensitivity of resistive and Hall measurements to local inhomogeneities: Finite-field, intensity, and area corrections," *J. Appl. Phys.* **116**(13), 133706 (2014).

## 1. Introduction

In the past decade many types of applications (*e.g.* gas sensors [1–3], transistors [4–6], OLEDs [7–9], corrosion protection [10–12], and photodetectors [13–15]), have been used to demonstrate the commercial potential of graphene. Now that high quality, large-scale CVD growth [16–18] and transfer [19–21] methods are becoming well established, the viability of graphene as a device component has become more realistic. However, in order to obtain reliable production of mass fabricated graphene devices, rapid quality assessment metrology is essential for process monitoring. Terahertz time-domain spectroscopy (THz-TDS) has been proven a possible candidate for large-scale electrical characterization of graphene and other two-dimensional materials [22]. With THz-TDS, it is possible to extract the conductivity  $\sigma$ , scattering time  $\tau$ , carrier concentration  $n$ , and carrier mobility  $\mu$  with a sub-millimeter spatial resolution. THz-TDS has various practical advantages as compared to contact-based electrical measurements: no need for polymers/solvents that are known to adversely affect the electrical properties of graphene [23]), high throughput for large areas [24] and possibility of identifying imperfections (*i.e.* grain boundaries) on the microscale [25]. Although it is established that  $\sigma$  can be derived from THz-TDS measurements, with this study, we confirm for the first time the accuracy and reproducibility between different laboratories for spatial mapping of graphene conductivity, which is a necessary step towards establishing a robust and reliable metrology platform. The confirmation of the accuracy of reflection-mode THz-TDS allows the method to be applied to a very large set of existing graphene devices/applications where transmission-mode THz-TDS is not compatible. The THz-TDS method is subject to standardization within the IEC.

## 2. Experimental setup and methods

### 2.1 Device fabrication via laser ablation

Wafer-scale graphene was grown by chemical vapor deposition (CVD) and transferred to a 100 mm diameter high-resistivity ( $>10$  k $\Omega$ ·cm) silicon wafer with a passivation layer of 165 nm Si<sub>3</sub>N<sub>4</sub>, as shown in Fig. 1 (a). Devices had electrical contacts evaporated *via* a shadow mask to enable van der Pauw measurements [Fig. 1 (b)]. Metal contacts had dimensions of 2.2 mm  $\times$  0.8 mm. Individual square devices of area 25 mm<sup>2</sup> were defined *via* laser ablation [26] as shown in Figs. 1 (c-d).

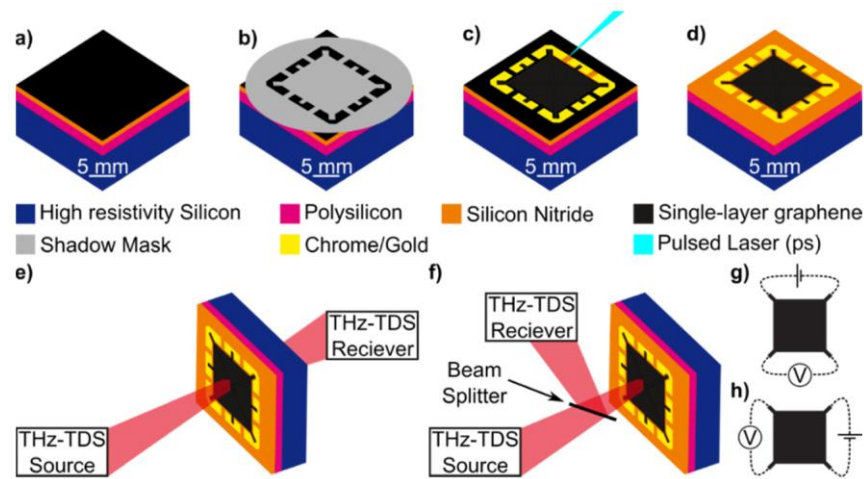


Fig. 1. a-d: Schematic showing fabrication of device. a) A silicon substrate with passivation layer of Si<sub>3</sub>N<sub>4</sub> has single-layer graphene transferred to it. b) A shadow mask is used to deposit metal contacts. c) A picosecond pulsed laser is used to selectively ablate the graphene d) Finished device. e) Schematic of THz-TDS in transmission mode. f) Schematic of THz-TDS in reflection mode. g) Schematic of measurement in the A configuration for vdP measurements. h) Schematic of measurement in the C configuration for vdP measurements.

## 2.2 Terahertz time-domain spectroscopy

THz-TDS in transmission mode [Fig. 1 (e)] was performed at the Department of Photonics Engineering at the Technical University of Denmark, using a Picometrix T-ray 4000 system described in detail elsewhere [27]. For transmission mode measurements the conductivity was extracted from the directly transmitted pulse after applying corrections for timing jitter as described in ref [28]. Scanning was performed with a static detector and scanning the samples in the x and y directions. Picometrix T-Ray 4000 system records data in a scanning window of 320 ps with 78 fs temporal resolution. The laboratory relative humidity was  $\approx 50\%$ . Measurement time was 20 minutes per sample. THz-TDS in reflection mode [Fig. 1 (f)] was performed using an ONYX measurement system which is a THz system working in reflection configuration, and co-developed with the Fraunhofer Institute for Industrial Mathematics at the company das Nano in Pamplona, Spain. Scanning was performed by movement of the sample in the y-axis and the source/receiver moving in the x-axis. The scanning window was 50 ps with 25 fs temporal resolution. Measurement time was 60 seconds per sample. The relative humidity was  $\approx 45\%$ . Both measurement protocols analyzed the sheet conductivity at 0.9 THz (corresponding to a beam with FWHM of approximately 400  $\mu\text{m}$ ), and used a 400  $\mu\text{m}$  step size for mapping. The Tinkham equation is used for the transmission coefficient from air to substrate through a thin conducting film. This is a valid approximation in the case where the thickness of the film  $t_{\text{film}} \ll \lambda / n_{\text{film}}$ , (where  $\lambda$  is the wavelength, and  $n_{\text{film}}$  is the film refractive index) which is a reliable approximation for atomically flat materials [29]. For pixel-to-pixel analysis, conductivity values within 1.2 mm of the metal contacts were excluded [30].

## 2.3 Van der Pauw measurements

Contact-based van der Pauw (vdP) measurements were performed at 30 °C [31] at the Department of Micro- and Nanotechnology, Technical University of Denmark. Sheet resistances ( $R_s$ ) were calculated using the vdP equation formula [32]:

$$e^{-\frac{\pi R_A}{R_s}} + e^{-\frac{\pi R_C}{R_s}} = 1 \quad (1)$$

where  $R_A$  and  $R_C$  are the measured resistances from the A configuration and C configuration, respectively, as shown in Fig. 1 (g-h). Assuming the geometry of the device is well-known, we can calculate the homogeneity factor

$$\beta = \frac{R_A}{R_C} \quad (2)$$

For a uniformly conducting square device with one contact positioned in each corner  $\beta=1$ .

### 3. Results and discussion

#### 3.1 Comparison of reflection and transmission modes of THz-TDS

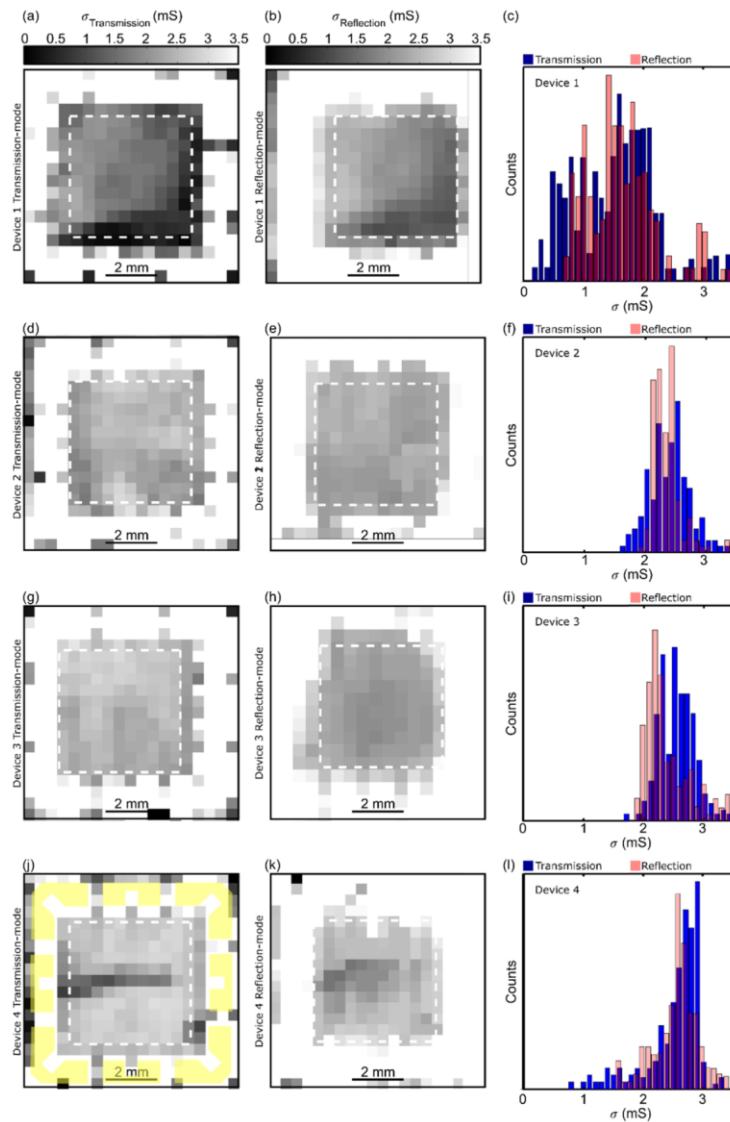


Fig. 2. THz-TDS conductivity maps for devices 1-4 for transmission (a,d,g,j) and reflection modes (b,e,h,k). Outline of metal contacts location shown in (j). Histograms comparing conductivity of devices 1-4 for transmission and reflection modes (c,f,i,l).

Figure 2 shows four devices with comparative conductivity maps. All devices originate from a single graphene growth, single transfer, and one laser ablation procedure. We have chosen four devices to be representative of different parts of the wafer, with two relatively homogenous (device 2 and 3) devices and two devices of lower homogeneity (device 1 and 4). In the following we focus on Device 1, as this is the most inhomogeneous device. Figure 2 a-b show the THz-TDS conductivity maps obtained by transmission and reflection modes respectively for Device 1. All pixels, including those which correspond to the metal contacts are treated using the same method. Although the Tinkham equation is likely inaccurate for metal of this thickness, all metal THz-TDS conductivity pixels are excluded from the following analysis and only included in Fig. 2 for completeness. For clarity, we have superimposed the contact pattern in yellow in Fig. 2. (j). Conductivity values in Fig. 2 above 3.5 mS are set to white. Qualitatively, we observed similar conductivity features in both maps, with a region of lower conductivity in the lower right corner. Figure 3 shows a pixel-to-pixel correlation between  $\sigma_{\text{transmission}}$  and  $\sigma_{\text{reflection}}$  for all devices. With Device 1, for conductivity values larger than 1.0 mS we observe an approximately 5% difference between the transmission and reflection methods, as extracted from a linear fit. For devices 2-4 we observe that the transmission measurements result in slightly higher values of  $\sigma$ , while the opposite is the case for Device 1.

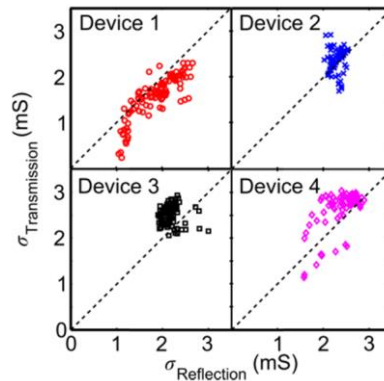


Fig. 3. Pixel-matched correlation plots of four devices of THz-TDS for transmission and reflection modes from Fig. 1.

### 3.2 Comparison of THz-TDS conductivity values with vdP measurements

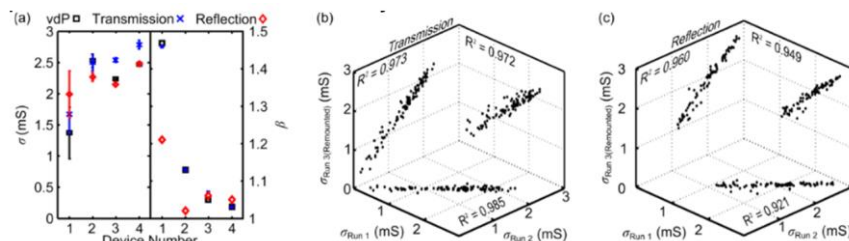


Fig. 4. a) Conductivity values (left) and homogeneity values  $\beta$  (right) for four devices obtained by van der Pauw measurements (black squares) and the median of 100 pixels maps of THz-TDS transmission (blue crosses) and reflection (red diamonds).  $\beta$  values from THz are extracted from a weighted average using to represent each configuration. b-c) Repeatability measurements of THz-TDS measurements of Device 1 for transmission and reflection mode, respectively. Run 1 is as shown in a. Run 2 was performed within two minutes of Run 1. Run 3 was performed immediately after the device was unmounted and remounted.

In order to determine the consistency of the THz-TDS results with respect to traditional conductivity measurements, the vdP method was used to calculate sheet conductivities [*cf.*

Eq. (1)]. The median  $\sigma_{\text{THz}}$  values for both measurement setups are compared with van der Pauw measurements [Fig. 4 (a)]. The median is used in place of the mean so that results are not so severely affected by pixels with very low conductivity, for example a scratch/isolating defect, which has been shown to affect the accuracy of the van der Pauw calculation [33]. Uncertainties were calculated from the standard deviation for THz-TDS and using the differences from the A and C configurations for vdP measurements, as described in ref [31]. We observe a spread of similar  $\sigma$  values with vdP values being approximately consistent with both THz-TDS data sets. We attribute the difference between measurements to minor changes in the ambient conditions between the three labs as well as contamination during handling and transferring. Ambient conditions are well known to affect the conductivity of graphene, such as temperature [34] and humidity [35], with each factor known to potentially contribute to a change in conductivity greater than the difference between our measurements. In order to confirm this for our device type, the vdP sheet conductivity was measured at various humidity levels, and between 25 – 35 °C as shown in Fig. 5. The relative humidity of the chamber was modified using a standard bubbler with deionized water. The humidity of the chamber was monitored using a Senisron humidity sensor, with electrical measurements performed as previously described [31]. The higher density of points around 30% rel. humidity corresponds to the ambient humidity of the vdP lab. We observe approximately a 1% change in  $\sigma$  over this temperature range; however, when the humidity is also varied we observe a far more significant change in  $\sigma$  of over 20%, consistent with the use of graphene as a humidity sensor [36]. Therefore, when the inevitable changes in humidity from day to day, and between laboratories are taken into account, ambient conditions can easily account for the observed laboratory-to-laboratory discrepancies.

If the conductivity of graphene without the influence of humidity is required, then a thermal treatment in a dry neutral gas would be required [23]. However, this would add significantly to the sample measurement time, when heating, annealing, cooling to measurement temperature, and temperature stabilization are taken into account. This process would increase the measurement time of a reflection-mode measurement from 1 minute to at least 1 hour, per device. In addition, the graphene conductivity would change in response to the ambient conditions when removed from the  $\text{N}_2$ . We intend the methods presented here to be a fast and accuracy measure of the graphene conductivity in lab ambient.

We note there are slight differences between the reflection-mode lab ( $\approx 45\%$ ) and the transmission-mode lab ( $\approx 50\%$ ). We therefore expect to observe lower conductivity values for our reflection-mode measurements, which is consistent with the data for devices 2-4 in Fig. 3. However, device 1 displays the opposite behavior.

We performed micro-Raman spectroscopy on our devices in order to determine the density of defects. Using a Thermo Scientific DXRxi each device was mapped with 5625 pixels with a 455 nm laser and with Raman peaks analyzed using the methods of [37]. The density of defects in graphene is routinely accessed *via* Raman spectroscopy by assessing  $I_{\text{D}}/I_{\text{G}}$ : the ratio of the intensity of the D-peak ( $\approx 1350 \text{ cm}^{-1}$ ) and the intensity of G-peak ( $\approx 1600 \text{ cm}^{-1}$ ) [38]. We observed medians of the  $I_{\text{D}}/I_{\text{G}}$  of 0.48, 0.16, 0.12 and 0.19 for devices 1-4 respectively, showing a larger defect density for device 1 relative to the other devices. An increase in defect density is highly related to the gas/humidity sensing properties as these defects act as binding sites for molecules which subsequently act as donors/acceptors and change the carrier concentration of the graphene device [39]. For graphene devices, the position of the charge neutrality point can also be influenced by the introduction of defects [40] and depending on the position of the charge neutrality point the same gas species can either increase or decrease the conductivity [39]. We therefore attribute the opposite change in conductivity for device 1 between the different labs to a higher defect density which creates a different chemisresistive response to humidity.

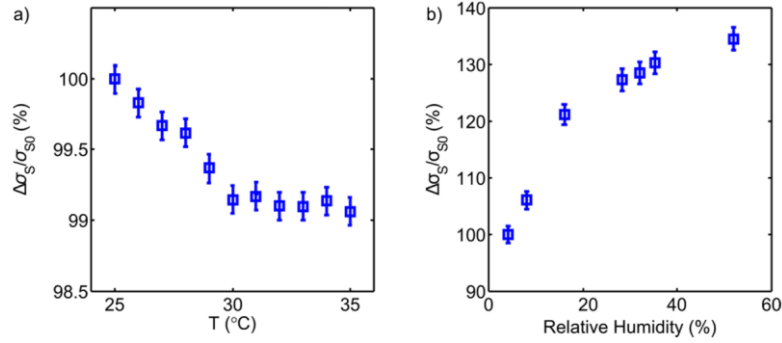


Fig. 5. a) Percentage change in vdP sheet conductivity for a range of temperatures at ~35% relative humidity in air. b) Percentage change in sheet conductivity for a range of relative humidities at 30 °C in air.

Much information is lost by taking a simple median of our THz data because the 100 pixel values from Fig. 2 are collapsed into a single conductivity value. The vdP method effectively takes a weighted average of the device conductivity, which can be visualized *via* a sensitivity map [1], which were here calculated by finite element simulation, using Comsol 5.2. Using the geometry from Fig. 6 (a), the A and C configuration are defined as in Fig. 1 (g-h), to be A: (Source,Drain,V,-V) = (1,2,3,4), and C: (Source,Drain,V,-V) = (3,4,1,2). Then, the x and y component of the current density ( $J_x$ ,  $J_y$ ) are extracted for each configuration and the prime configurations ( $A_{\text{Prime}}$ : (Source,Drain,V,-V) = (3,4,1,2) and  $C_{\text{Prime}}$ : (Source,Drain,V,-V) = (1,3,2,4)). The normalized sensitivity  $S$  for a single configuration can then be calculated using [41]:

$$S = J_x \cdot J_{x\text{Prime}} + J_y \cdot J_{y\text{Prime}} \quad (3)$$

which is normalized using  $\iint S \, dx dy = 1$ . The example of the A configuration is shown in Fig. 6 (b), with the C configuration being equivalent, except rotated 90°. The dual configuration/vdP sensitivity is calculated using  $S_{\text{vdP}} = \frac{S_A + S_C}{2}$  where  $S_A$  and  $S_C$  are the sensitivities for the A and C configurations respectively, and is shown in Fig. 6 (c).

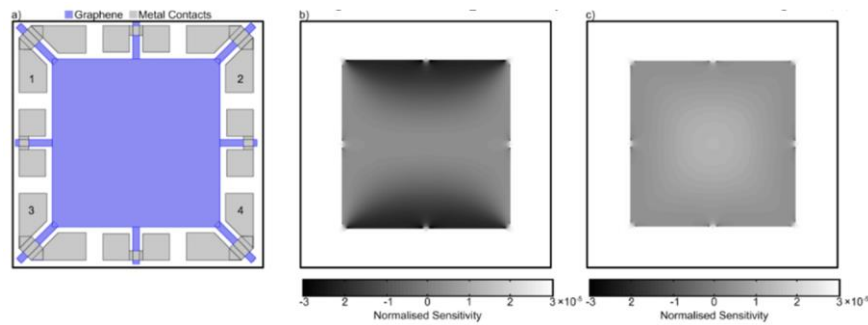


Fig. 6. Sensitivity map calculations *via* finite element simulations. a) Design input showing graphene areas in blue and metal contacts in grey. A configuration defined as Source: Contact 1, Drain: Contact 2, V + probe: 3, V- probe: 4. C configuration defined as Source: Contact 3, Drain: Contact 4, V + probe: 1, V- probe: 2. b) Normalized sensitivity map for the A configuration measurement. c) Normalized sensitivity map for the dual configuration vdP measurement.

We show sensitivity maps for our devices calculated using finite element simulations in Fig. 5 for both the vdP corrected [Fig. 6 (c)] and single-configuration sensitivity [Fig. 6 (b)].

The single configuration sensitivity is non-symmetrical, with two edges of the device contributing more significantly to the measured conductivity.

In order to make a more representative comparison between THz maps and vdP measurements, the normalized sensitivity map from Fig. 6 (b) was used as a weighted matrix to create virtual single configuration THz-TDS conductivity maps. The medians of the single configuration THz-TDS conductivity maps can then be used with Eq. (2) to determine the homogeneity factor  $\beta$ . Because  $\beta$  depends only on the geometry of the device, it should be independent from the ambient condition conductivity variations discussed above. The calculated homogeneity factor for all devices are shown in Fig. 4 (a), with six out of eight of the THz-derived  $\beta$  values having very good agreement with the vdP-based  $\beta$ . The agreement in  $\beta$  values strongly suggests that all three methods are measuring the same  $\sigma$  landscape. The results shown in Fig. 4 (a) suggest that the conductivity maps measured using THz-TDS are consistent with traditional contact-based methods within the uncertainties associated with the variations expected when graphene is exposed to ambient conditions.

### 3.3 Measurement-to-measurement variations in THz-TDS conductivity

In order to investigate the measurement-to-measurement variation within the same laboratory, measurements of devices were repeated for both THz-TDS methods in the following order. A device is mounted and measured (Run 1), and then immediately re-measured (Run 2). The device is then unmounted, immediately remounted and measured again (Run 3). The sample and any atmospheric conditions mentioned above should not significantly change in this time and any differences can be attributed to systemic measurement errors. The results for transmission and reflection for Device 1 are shown in Fig. 4 (b) and 4 (c) respectively. When comparing the measured conductivities, we observe only minor variations in correlation of the repeated and reproduced measurements for both transmission and reflection mode. We observe lower values for  $R^2$  for reflection-mode measurements for all devices, which is attributed to the slightly lower resolution associated with a 20-times faster scan rate. The median conductivities measured in transmission mode was 1.67 mS, 1.70 mS and 1.63 mS and in reflection mode 1.99 mS, 2.09 mS and 2.02 mS. Overall, we observe at most 5% error in median conductivity between intra-laboratory runs, which is simply attributed to systematic and/or random measurement errors, and is a smaller effect than the offset associated with atmospheric conditions and historic surface contamination.

We suggest the following methodologies in order to reduce errors associated with THz-TDS measurement of graphene conductivity and to allow for more meaningful inter- and intra-lab comparisons. We recommend that the recent environmental history of the device is well known and documented. Moving a device from an environment with high humidity to a lab with controlled low humidity will significantly affect any graphene conductivity experiment. Even if the measurements are performed in dry  $N_2$ , without a thermal treatment surface absorbents will still be present [23]. In addition, laboratory temperature should also be controlled, or at least recorded. In addition, exposure to oxidizing or reducing gases should be avoided as these are well known to affect graphene conductivity [39] and are also known to not desorb without thermal treatment [35].

## 4. Conclusion

We find that both reflection and transmission modes of THz-TDS are both accurate and precise methods for extracting graphene conductivity, and show that the methods are interchangeable within measurement uncertainties. The conductivity results obtained were comparable with traditional vdP measurements, even when the device had significant inhomogeneities. Our results suggest that THz-TDS is a powerful tool for electrical metrology on large scale graphene, with output ranging from a single value average  $\sigma$ , to a high-density spatial map revealing the presence of any inhomogeneities or insulating defects.

Different factors contribute to variations in measured parameters between different experimental runs. For the case of large-scale graphene measured with THz-TDS, a variation of up to 15% of the median conductivity was observed for laboratory-to-laboratory measurements, and up to 5% for inter-laboratory measurements. Inter-laboratory error was attributed to systematic and/or random errors in measurement/analysis and that laboratory-to-laboratory measurement uncertainty can be attributed to the expected variations in graphene conductivity due to changes in ambient temperature and humidity. We recommend that the recent history of exposure to humidity/oxidizing or reducing gases of devices is monitored and recorded, as these surface adsorbents can significantly affect the conductivity of graphene.

### **Funding**

DNRF103 CNG, HC Ørsteds Foundation; Villum Fonden project no.VKR023117; H2020 European Project No. 692527; EC Graphene FET Flagship contract number 604391.

### **Acknowledgments**

We thank the Nanocarbon group at DTU Nanotech for useful guidance as well as the staff at DTU Danchip for valuable fabrication discussions.